

Broadband loop gap resonator for nitrogen vacancy centers in diamond

E. Eisenach,^{1,2, a)} J. Barry,² R. Rojas,² L. Pham,² D. Englund,¹ and D. Braje²

¹⁾Department of Electrical Engineering and Computer Science, Massachusetts Institute of Technology, Cambridge, MA 02139, USA

²⁾MIT Lincoln Laboratory, Lexington, MA 02421, USA

(Dated: 27 April 2018)

We present an S-band tunable loop gap resonator (LGR) providing strong, homogeneous, and directionally uniform broadband microwave (MW) drive for nitrogen-vacancy (NV) ensembles. With 42 dBm of input power, the composite device provides drive field amplitudes approaching 5 G over a circular area $\gtrsim 50 \text{ mm}^2$ or cylindrical volume $\gtrsim 250 \text{ mm}^3$. The wide 80 MHz device bandwidth allows driving all eight NV Zeeman resonances for bias magnetic fields below 20 G. For pulsed applications the device realizes percent-scale microwave drive inhomogeneity; we measure a fractional root-mean-square inhomogeneity $\sigma_{\text{rms}} = 1.6\%$ and a peak-to-peak variation $\sigma_{\text{pp}} = 3\%$ over a circular area of 11 mm^2 , and $\sigma_{\text{rms}} = 3.2\%$ and $\sigma_{\text{pp}} = 10.5\%$ over a larger 32 mm^2 circular area. We demonstrate incident MW power coupling to the LGR using multiple methodologies: a PCB-fabricated exciter antenna for deployed compact bulk sensors and an inductive coupling coil suitable for microscope-style imaging. The inductive coupling coil allows for approximately 2π steradian combined optical access above and below the device, ideal for envisioned and existing NV imaging and bulk sensing applications.

I. INTRODUCTION

The nitrogen-vacancy (NV) defect center in diamond is employed in a number of wide-ranging applications from quantum information processing^{1,2} to tests of fundamental physics^{3,4} to quantum sensing and metrology. In particular, NV-based quantum sensors have demonstrated utility in a broad variety of modalities, including magnetometry⁵, electrometry^{6,7}, nanoscale NMR^{8–10}, single proton and single protein detection^{11,12}, thermometry^{13,14}, time-keeping¹⁵, and more^{16–18}. Each of these applications takes advantage of one or more principal features of the NV center: all-optical initialization and readout^{19,20}, long coherence time under ambient conditions^{21–24}, nanoscale size^{25,26}, or fixed crystallographic axes^{27–29}. However, with notably few exceptions^{30,31}, *all* NV applications rely on the ability to coherently manipulate the NV ground-state spin via resonant microwave (MW) driving. A number of these applications additionally require generation of strong and uniform MW fields over large areas ($\gtrsim 10 \text{ mm}^2$) or volumes ($\gtrsim 30 \text{ mm}^3$)^{32–36}, a difficult task that benefits significantly from improvements to standard MW delivery methods. In this work, we discuss the design considerations for a suitable MW delivery mechanism, fabricate a hole-and-slot type loop gap resonator (LGR), and evaluate its performance for NV applications.

Multi-channel imagers and highly sensitive, single-channel bulk sensors are two examples of application modalities that benefit significantly from large detection areas and volumes, respectively. In the case of multi-channel imagers, increasing the detection area extends the measurement field-of-view, whereas for bulk sensors, increasing the detection volume can considerably enhance measurement sensitivity. For example, the

shot-noise-limited sensitivity of an NV magnetometer is approximately given by⁵

$$\eta \approx \frac{\hbar}{g_s \mu_B} \frac{1}{C \sqrt{\beta \tau}} \frac{1}{\sqrt{N}}, \quad (1)$$

where N is the number of NV sensors, τ is the duration of the measurement, C is the measurement contrast, β is the number of photons collected per NV per measurement, μ_B is the Bohr magneton, $g_s \approx 2$ is the ground state NV⁻ Landé g-factor, and \hbar is the reduced Planck constant. The magnetic sensitivity can be improved by increasing N , achievable through higher NV density or larger detection volumes. However, NV ensemble coherence times, which limit the optimal measurement time τ ,

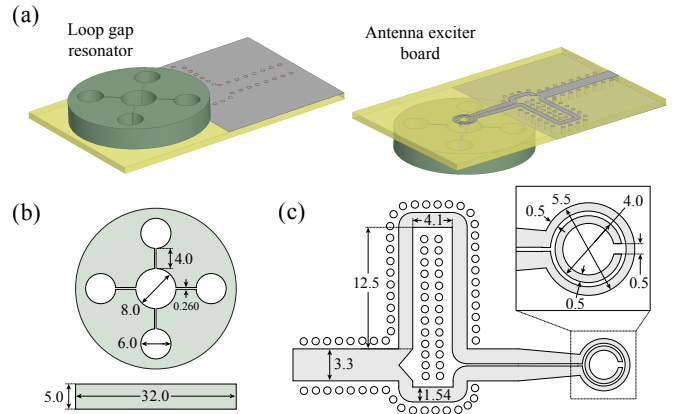


FIG. 1. (Color online) **Loop gap resonator and exciter antenna board.** (a) The metallic resonator employs a five-loop four-gap architecture. Microwaves are coupled into the LGR via the exciter antenna, which is fabricated on a printed circuit board. (b) Line drawing of LGR. (c) Exciter antenna. A feedline, 50:50 power splitter, and balun (balanced/unbalanced) feed the split ring resonator, which is coupled to the LGR. All dimensions are in mm. Optional mounting holes and radial access port for laser excitation are not shown.

^{a)}Electronic mail: eisenach@mit.edu

depend inversely on NV density⁵. As a result, there is a practical upper bound on the NV density after which further sensitivity enhancements are attained by increasing the detection volume. For application modalities such as those discussed above, the MW field requires both high power and uniformity in order to achieve high-fidelity quantum state manipulation over the full measurement region.

Standard approaches to applying MW drive to NV ensembles or other solid state spin systems include shorted coaxial loops^{36,37}, microstrip waveguides^{38,39}, coplanar waveguides⁴⁰, and other coaxial transmission line approaches⁴¹. While such broadband approaches allow arbitrary drive frequency, the lack of resonant enhancement forces a compromise between the volume addressed (assuming a fixed homogeneity is required) and MW field strength, denoted B_1 . Planar lumped-element resonators such as split-ring resonators^{39,42}, planar-ring resonators^{43,44}, omega resonators⁴⁴⁻⁴⁷, and patch antennas³⁹ forego the flexibility of broadband solutions in favor of resonantly enhanced magnetic fields, thus enabling MW driving over larger regions. For example, the split-ring resonator presented by Bayat *et al.* achieves a MW field strength of $B_1 = 5.6$ G and a fractional root-mean-square inhomogeneity of $\sigma_{\text{rms}} \approx 4.4\%$ over a ~ 1 mm² area⁴². However, such planar structures are ill-suited to providing good B_1 homogeneity away from the plane of fabrication. The community has addressed this shortcoming by employing a variety of three-dimensional resonators. Enclosed metallic cavity resonators⁴⁸, enclosed dielectric resonators⁴⁹⁻⁵¹, open dielectric resonators⁵², and certain three-dimensional lumped element resonators⁵³ all allow for good homogeneity over large volumes but unfortunately offer little to no optical access. As all-optical initialization and read-out is a primary benefit for many solid-state spin systems, including NV-diamond⁵⁴, such a trade-off is incompatible with many existing and envisioned applications⁵⁵.

To address this current shortcoming we present a three-dimensional tunable loop gap resonator. The design is based on the anode block of a hole-and-slot-type cavity magnetron and, similar to certain devices discussed above, utilizes resonant enhancement to achieve the desired MW drive strengths over large areas (>50 mm²) or volumes (>250 mm³). The design has an open geometry; for interrogation volumes centered within the LGR, approximately half of the 4π solid angle remains optically accessible. Importantly, for currently semi-standardized commercial diamond plates (2-4.5 mm side lengths with 0.5 mm thickness) this solution allows maximal access to the diamond's large front and back faces. The open access, good homogeneity, and high B_1 fields over the 8 mm diameter by 5 mm thickness cylindrical volume make the device well-suited both for wide-field magnetic imaging—applicable to studies of living systems^{14,16,32,56}, early earth rocks or meteorites^{33,34}, single cells⁵⁷, electronic devices⁵⁸, etc.—and for single-channel bulk sensing^{16,35,36,59,60} targeting geosurveying, magnetic anomaly detection, space weather monitoring, etc.

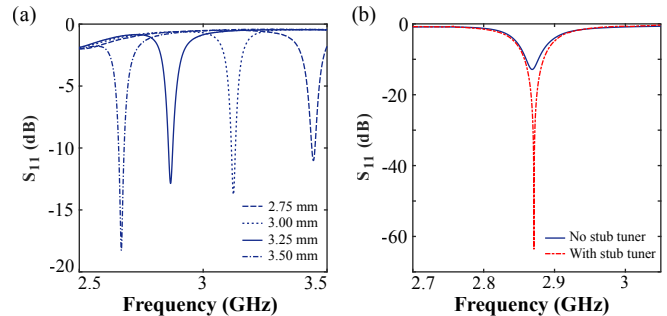


FIG. 2. (Color online) **Frequency tuning and impedance matching of LGR composite device.** (a) The resonant frequency f_0 is adjusted by translating the sapphire shims in the four capacitive gaps. In the absence of a stub tuner, the LGR composite device exhibits S_{11} values between -10 and -20 dB from 2.5 to 3.5 GHz, indicating $\gtrsim 90\%$ of power delivered to the LGR composite device contributes to B_1 in this range. (b) Nearly perfect critical coupling can be achieved with a stub tuner, allowing practically all incident MW power to contribute to B_1 .

II. LOOP GAP RESONATOR DESIGN AND FABRICATION

A standard hole-and-slot LGR with n outer loops may be approximated as n coupled LC resonators oscillating in tandem⁶¹. Circulating currents around the central and outer loops create a total inductance L , given by⁶¹⁻⁶³

$$L \approx \frac{L_c n L_o}{n L_o + L_c}, \quad (2)$$

where L_c and L_o denote the inductance of the central loop and of a single outer loop, respectively. Similarly, the n narrow capacitive gaps create a total capacitance C , which is given by⁶¹⁻⁶³

$$C \approx \frac{\epsilon_r \epsilon_0 A}{nd}, \quad (3)$$

where A and d are the capacitive gap side wall area and separation, respectively. The resonant frequency of the LGR is therefore given by

$$f_0 = \frac{1}{2\pi\sqrt{LC}}. \quad (4)$$

In practice, the central loop diameter is set to ~ 5 -10 mm, corresponding to the typical size of a diamond plate, whereas d is limited by practical machining tolerances and ϵ_r by physically available materials. The capacitive gap area A is constrained by the dual LGR design objectives of (i) maintaining optical accessibility, which limits the thickness of the LGR device, and (ii) bounding f_0 above the target resonant frequency in order to allow for further tuning via shims (discussed below). Additionally, while increasing the number n of loops and gaps can improve B_1 uniformity⁶⁴, this approach results in a denser mode spectrum⁶² and increases the likelihood of cross-mode excitations deleteriously altering the field distribution within the central loop. As a compromise, our design employs $n = 4$ outer loops [Fig. 1(b)], thus allowing for

sufficient uniformity while locating the closest eigenmode more than 1.5 GHz below the TE_{01} eigenmode.

The LGR detailed in this work consists of a central loop of radius $r_c = 4$ mm surrounded by $n = 4$ symmetrically arranged outer loops of radius $r_o = 3$ mm, as shown in Fig. 1(b). The outer loops return magnetic flux to the central loop and therefore oscillate antisymmetrically with the central loop (180° out of phase). The side walls of the capacitive gaps are separated by $d = 260$ μm . With these dimensions, Eqns. 2 and 3 predict $L = 8.7$ nH and $C = 0.17$ pF respectively, resulting in an expected resonant frequency for the naked air-gapped LGR of $f_0 = 4.1$ GHz, approximately 1.2 GHz above the NV resonance frequencies. For comparison, the measured f_0 for the air-gapped resonator is in the 4.6–4.9 GHz range.

The LGR resonant frequency f_0 is additionally tuned by inserting and translating dielectric shims in the LGR's capacitive gaps, thereby increasing total capacitance C until f_0 overlaps the NV resonance frequencies as desired. As shimming material, we employ 200 μm thick C-plane sapphire, which is commercially available in semiconductor grade 50.8 mm diameter wafers, can be cut on standard wafer dicing saws, has a high relative permittivity of $\epsilon_r = 11.5$ parallel to the C-plane⁶⁵ (allowing for a large tuning of f_0), and exhibits low dielectric loss ($\text{Tan } \delta < .0001$ at 3 GHz^{65,66}). The sapphire shims are cut to lengths longer than the $l_c = 4$ mm radial length of the capacitive gaps and wedged into the $n = 4$ capacitive gaps with teflon thread tape. These sapphire shims are then translated radially until the desired value of f_0 is attained. The shims are always positioned so that excess shim length extends into the outer rather than the central loop, in order to minimally perturb the central loop B_1 field. Simulations further suggest that radially symmetric shim configurations produce the best B_1 field homogeneity, as asymmetries in shim placement perturb the desired TE_{01} field distribution. Insertion and removal of diamonds in the LGR composite device typically leaves f_0 unchanged, as the large electric fields of the TE_{01} mode are predominantly confined to the capacitive gaps (see Appendix B 2).

The LGR is fabricated via wire electron discharge machining, which is well-suited for producing the tight tolerances and vertical side walls required for the narrow $d = 260$ μm capacitive gaps. A titanium alloy (Ti-6Al-4V) was chosen as the resonator cavity material. The lower conductivity of this alloy compared to that of copper ($\sigma_{\text{Ti}} = 5.7 \pm 0.1 \times 10^5$ S/m vs. $\sigma_{\text{Cu}} = 5.9 \times 10^7$ S/m) allows for a broader resonance with a 3dB bandwidth $\Delta_{3\text{dB}} = 80$ MHz, sufficient to address all eight NV resonances for bias magnetic fields B_0 up to ~ 20 G. This 80 MHz bandwidth corresponds to a loaded quality factor $Q_L \equiv f_0/\Delta_{3\text{dB}} \approx 36$ when the LGR is critically coupled to the driving source. The LGR may be optionally fit with a radial access hole (for laser excitation of the NV ensemble) and three #2-56 mounting holes, which affix the LGR to an exciter antenna, discussed next.

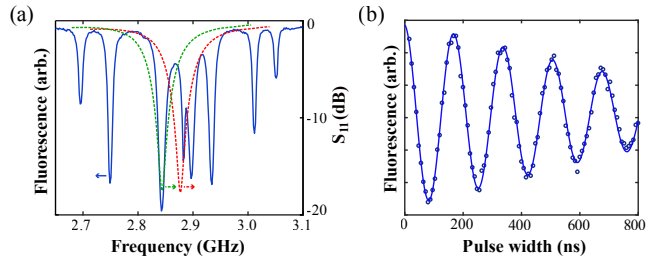


FIG. 3. (Color online) **LGR driving of an NV ensemble.** (a) NV electron spin resonance spectrum (—) under application of bias field B_0 . The bias field allows individual addressing of all eight NV resonances, arising from the combination of the two allowed magnetic dipole transitions with the four possible NV orientations. The NV hyperfine structure is obscured by MW power broadening and the contrast variation between the NV resonances is attributed primarily to the S_{11} line-shape. The S_{11} parameter is shown before (---) and after (---) shifting the LGR resonant frequency f_0 to the target NV resonance. Arrows indicate corresponding y axes. (b) Typical data depicting Rabi oscillations under MW excitation at the target NV resonance frequency indicated in (a). Data (\circ) is fit (—) to an exponentially decaying sinusoid.

III. LOOP GAP RESONATOR COUPLING AND EXCITER ANTENNA BOARD

Incident MW power P is inductively coupled into the LGR by an exciter antenna, composed of a split ring resonator that is differentially driven by a microstrip balun, as shown in Fig. 1(c). The differential driving mitigates common-mode noise on the two traces, which might otherwise couple to the split-ring resonator. Although the microstrip balun is designed to match the feed-line and the split ring component of the exciter antenna at frequencies near 2.87 GHz, good matching is achieved from 2.5 GHz to 3.5 GHz as well. For drive frequencies between 2.5 and 3.5 GHz, the exciter antenna board couples more than 90% of incident MW power into the LGR, as shown in Fig. 2(a). For a specific fixed frequency, the impedance matching may be further optimized by inserting a stub tuner between the MW source and the exciter antenna board, as shown in Fig. 2(b).

A via shield along a portion of the balun helps reduce interference and cross-talk between traces, controls the trace impedance, and reduces radiative losses along the balun's π -phase delay arm. The exciter antenna is fabricated from 1 oz. copper trace with immersion silver finish on 1.524 mm thick dielectric (Rogers, RO4350B). Although the proximity of the split ring resonator perturbs the field distribution inside the LGR, both simulations and measurements suggest this effect is small and not the dominant inhomogeneity source (see Section IV). For applications intolerant of such perturbations or those requiring maximal diamond optical access, we achieved similar success inductively coupling a small coil of radius $\approx r_o$ to one of the outer loops⁶⁷, where the coil is translated (via mechanical stage) until the desired coupling is achieved. We expect this coupling method to be particularly suitable for laboratory or clinical imaging applications.

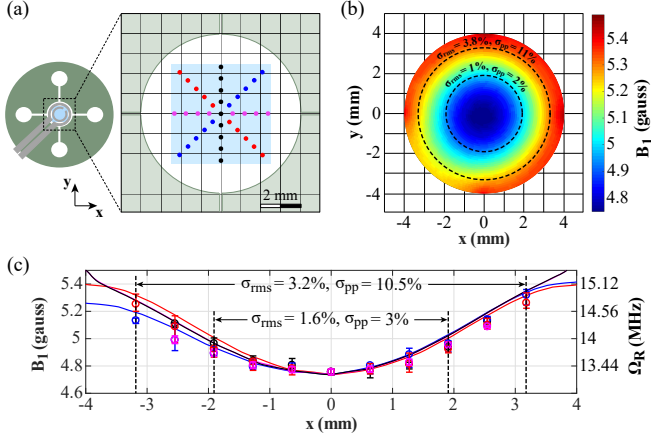


FIG. 4. (Color online) B_1 field uniformity of LGR composite device. (a) An NV-containing $4.5 \text{ mm} \times 4.5 \text{ mm}$ diamond plate is placed in the LGR central loop, and the Rabi frequency is measured where indicated ($\bullet, \circ, \circ, \bullet$) to characterize B_1 . (b) Simulations suggest the B_1 field distribution should be approximately radially symmetric, with the leading order deviation resulting from the exciter antenna. Dashed lines indicate the 32 mm^2 and 11 mm^2 areas within which the B_1 field uniformity is evaluated. (c) B_1 field measurements ($\circ, \circ, \circ, \circ$) at the points depicted in (a) and simulations ($-$, $-$, $-$, $-$) along each locus of points are in good agreement. Error bars indicate 1-sigma uncertainty for the B_1 measurement. Dashed lines indicate the radial boundaries of the 32 mm^2 and 11 mm^2 areas over which B_1 field uniformity is evaluated. The measured B_1 uniformity is given for each area.

IV. LOOP GAP RESONATOR PERFORMANCE

The strength and homogeneity of B_1 within the LGR central loop is evaluated employing standard NV techniques, as described in detail in Ref.⁶⁸ and elsewhere^{69,70}. A $\{100\}$ -cut diamond plate containing $\sim 1 \times 10^{14} \text{ NV/cm}^3$ is mounted at the center of the LGR with the $\langle 100 \rangle$ crystallographic axis collinear with the LGR axis. A rare earth magnet creates a static magnetic bias field B_0 , which shifts the energies of the $m_s = \pm 1$ ground-state Zeeman sublevels. The energy shifts are given to first order by⁵

$$\Delta E \approx g_s \mu_B m_s \vec{B}_0 \cdot \hat{n}_i, \quad (5)$$

where \hat{n}_i denotes a unit vector oriented along one of the four diamond crystallographic axes. By judicious choice of \vec{B}_0 , all eight energy levels and associated $m_s = 0 \leftrightarrow m_s = \pm 1$ magnetic dipole transitions can be isolated as shown in Fig. 3(a). The resonator is tuned to excite a single NV transition, yielding Rabi oscillations [Fig. 3(b)]. The data is fit to an exponentially decaying sinusoid in order to extract the Rabi frequency Ω_R , from which the magnitude of B_1 can be calculated as

$$B_1 = \sqrt{3} \frac{\hbar \Omega_R}{g_s \mu_B}. \quad (6)$$

In this geometry, the B_1 field is oriented along the $[100]$ crystallographic axis of the diamond, degenerately offset from all four NV axis orientations by half the tetrahedral

bond angle $\theta_{tet}/2 = \text{ArcCos} \frac{1}{\sqrt{3}} \approx 54^\circ$. NV Rabi oscillations are driven by the B_1 field component transverse to the NV symmetry axis, reducing the Rabi frequency by $\sqrt{2/3}$ ⁴³. Accounting for the rotating wave approximation introduces another factor of $1/\sqrt{2}$, resulting in the conversion factor $\sqrt{3}$ in Eq. 6. To ensure \vec{B}_0 is consistent for all measurements across the LGR central loop [Fig. 4(a)], the confocal excitation volume is held fixed with respect to the B_0 -generating permanent magnet, and the diamond and LGR composite device are translated together. We employ a long working distance objective (Mitutoyo 378-803-3, M Plan Apo $10 \times \text{NA}=0.28$) to collect the NV fluorescence; the 34 mm working distance is necessary to minimize perturbation of the B_1 field by the metal objective housing. Future NV wide-field imaging applications may require ceramic-tipped objectives.

Application of incident MW power $P \approx 42 \text{ dBm}$ yields an axially oriented B_1 at the center of the LGR with magnitude 4.7 G . The corresponding Rabi frequency $\Omega_R = 2\pi \times 7.7 \text{ MHz}$ for NV centers oriented at half the tetrahedral bond angle relative to the LGR axis. Qualitatively, as shown in Fig. 4(c), B_1 displays a minimum at the LGR center, increases in magnitude with increasing radial displacement from the center, and is approximately radially symmetric. The best homogeneity is therefore expected at the LGR center.

The B_1 field uniformity is quantitatively characterized using both the fractional root-mean-square inhomogeneity σ_{rms} and the fractional peak-to-peak variation $\sigma_{\text{pp}} = [B_1^{\text{max}} - B_1^{\text{min}}]/B_1^{\text{average}}$. The use of both metrics facilitates comparison with alternative existing designs. Over a 32 mm^2 circular area axially centered in the LGR central loop, we observe $\sigma_{\text{rms}} = 3.2\%$ and $\sigma_{\text{pp}} = 10.5\%$, as shown in Fig. 4(c). Over a smaller 11 mm^2 circular area, we observe $\sigma_{\text{rms}} = 1.6\%$ and $\sigma_{\text{pp}} = 3\%$.

The LGR performance is modeled using a commercial finite element MW simulation package (Ansys, HFSS). Simulations include the exciter antenna board, which causes a small perturbation to the otherwise radially symmetric field [Fig. 4(b)]. The simulation predicts $B_1 \approx 4.8 \text{ G}$ at the LGR center with incident MW power $P = 42 \text{ dBm}$. Within a 32 mm^2 circular area centered in the LGR central loop, simulations indicate $\sigma_{\text{rms}} = 3.8\%$ and $\sigma_{\text{pp}} = 11\%$, whereas in a smaller 11 mm^2 circular area, simulations indicate $\sigma_{\text{rms}} = 1\%$ and $\sigma_{\text{pp}} = 2\%$. These simulation results are in good agreement with the measurements above.

As a three-dimensional cavity resonator, the LGR provides better axial field uniformity than planar-only geometries^{50,52,53}. For example, for a 3.14 mm^3 cylindrical volume (1 mm radius disk with 1 mm thickness), simulations yield $\sigma_{\text{rms}} = 0.8\%$, $\sigma_{\text{pp}} = 3.7\%$ and an average B_1 of 4.8 G (see Appendix B3).

V. DISCUSSION

The device presented here exhibits further benefits which we now discuss, along with extensions tailored for specific applications. For example, for ubiquitously employed pulsed measurement protocols, a short ring-down

time τ_{ring} (i.e., B_1 field $1/e$ decay time) is necessary for high-fidelity pulse shape control. Although techniques to compensate for long ring-down times are effective^{71–73}, shorter native values of τ_{ring} are nonetheless generally desired^{74,75}. The observed loaded quality factor $Q_L = 36$ corresponds to a ring-down time of $\tau_{\text{ring}} = 4$ ns (see Appendix B), making the device suitable for standard pulsed protocols^{76,77}.

Due to square-root scaling of B_1 with incident MW power ($B_1 \propto \sqrt{P}$), higher power handling can allow for stronger B_1 fields. The non-planar resonator design allows for otherwise higher incident MW powers as currents circulate over an extended 2D surface (versus the 1D edge for a planar structure). Further, the metallic LGR thermal mass and thermal conductivity allow efficient heat transfer and sinking, resulting in improved device stability and power handling. Although the latter was not tested, the LGR composite device is expected to allow > 100 W for CW and pulsed operation, limited by dielectric breakdown of air in the 260 μm capacitive gaps. Should available MW power be constrained, stronger B_1 can be achieved by fabricating the LGR from a more electrically conductive material (e.g. silver or copper) at the expense of bandwidth. In such circumstances, the bandwidth can be continuously adjusted above its minimum value by over-coupling the resonator (at the expense of reduced Q_L).

While the presented LGR is 5 mm thick, the fundamental hole-and-slot approach is expected to be feasible for a variety of thicknesses. A thicker device will provide better field uniformity at the expense of optical access. In contrast, for applications requiring MW delivery over a thin planar volume, we expect the LGR can be fabricated via deposition on an appropriate insulating substrate, as discussed in Refs.^{44,78}. We have found semi-insulating silicon carbide²⁹ suitable due to the material's high thermal conductivity (≈ 490 W/(m*K)^{79,80}, high Young's modulus, moderate cost and wide availability in semi-conductor grade wafers. Our simulations suggest the planar LGR approach can offer modest improvements in B_1 homogeneity over split ring resonators.

Although the exciter antenna (see Section III) facilitates a compact, vibration-resistant, and portable device, this component introduces non-idealities in both field uniformity and optical access. As similar scattering parameters are obtained by inductively coupling a small coil to one of the LGR outer loops, this latter solution may find favor for applications requiring maximal optical access and, furthermore, requires no PCB fabrication.

In this work, we demonstrated a broadband tunable LGR allowing application of strong homogeneous MW fields to an NV ensemble. The LGR demonstrates a dramatic improvement over prior MW delivery mechanisms, both improving on and spatially extending MW field homogeneities. We expect the device to be useful for bulk sensing^{16,35,36,59,60} and particularly imaging applications^{16,32–34,57,81,82}, due to the optical access allowed by the LGR composite device both above and below the diamond.

VI. ACKNOWLEDGMENTS

The authors would like to thank P. Hemmer, M. Newton, C. McNally, and S. Alsid for helpful discussions, and G. Sandy for resonator design simulations. E. Eisenach was supported by the National Science Foundation (NSF) through the NSF Graduate Research Fellowships Program. Any opinions, findings, conclusions, or recommendations expressed in this material are those of the author(s) and do not necessarily reflect the views of the U.S. Government.

Appendix A: Appendix A

1. The NV Center in Magnetometry

The negatively-charged NV color center (NV⁻) is a deep band gap impurity within the diamond crystal lattice [Fig. A.1(a)]. The point defect's C_{3v} symmetry results in a 3A_2 spin-triplet ground state and a 3E spin-triplet excited state, separated by a zero phonon line (ZPL) of 637 nm⁸³. Spin-spin interactions give rise to a zero-field splitting in the ground-state spin triplet, shifting the $m_s = \pm 1$ states with respect to the $m_s = 0$ state by $D_{\text{gs}} \approx 2.87$ GHz [Fig. A.1(b)]. In the presence of a static magnetic field B_0 , the $m_s = \pm 1$ sublevels experience Zeeman splitting proportional to the projection of the magnetic field along the NV symmetry axis. Above-band optical excitation (typically performed with a 532-nm laser) results in phononic relaxation of the NV spin within the 3E excited state, followed by fluorescent emission in a broad band. While these optical transitions are generally spin-preserving, an alternate decay path through a pair of metastable singlet states (1A_1 and 1E) results preferential relaxation from the $m_s = \pm 1$ excited states to the $m_s = 0$ ground state that is non-radiative in the typical 637–800 nm fluorescence band. This behavior under optical excitation has two major consequences: (1) an optical means of polarizing the NV spin, and (2) optical detection via spin-state-dependent fluorescence intensity.

Measurement of the NV electron spin resonance (ESR) spectrum can be performed by sweeping the carrier fre-

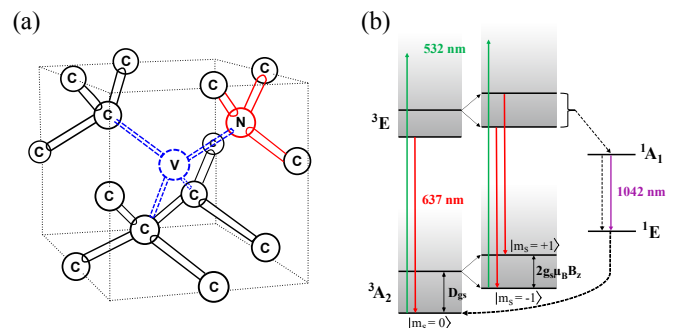


FIG. A.1. (Color online) **The NV center structure.** (a) The NV electronic energy level structure. (b) Example of one NV center orientation within the diamond crystal structure.

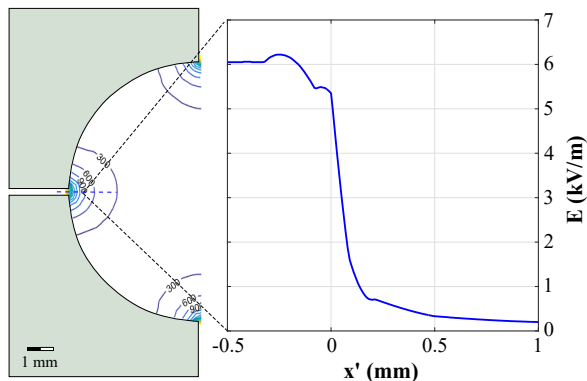


FIG. B.1. (Color online) **Simulated electric field magnitude E in vicinity of LGR capacitive gap.** Inset depicts the electric field magnitude E as a function of distance from the capacitive gap with $x' = 0$ mm corresponding to the plane of the central loop-gap interface. Observed subfeatures between -0.3 mm and 0.2 mm arise from fringing fields, and are complicated by the 260 μm gap only being partially filled by the 200 μm thick sapphire.

quency of the MW drive field and monitoring NV fluorescence in the visible band. Generally, the continuous optical excitation pumps the NV spin population into the more fluorescent $m_s = 0$ state; however, when the carrier frequency is resonant with an NV spin transition, the NV spin population is cycled into an $m_s = \pm 1$ state, causing decreased fluorescence intensity, which appears as a dip in the ESR spectrum^{84,85}. Since the NV symmetry axis may be aligned along one of four possible crystal-defined orientations—each orientation being equally thermodynamically likely in low strain diamond—the ESR spectrum can contain up to eight distinct non-degenerate NV resonances, which probe different field components. The different orientations act as basis vectors, which collectively span the space and allow the total vector field to be reconstructed⁸⁴.

Appendix B: Appendix B

1. Cavity Ring-down Time

The $1/e$ cavity ring down time of the B_1 field is^{74,75}

$$\tau_{\text{ring}} = \frac{Q}{\pi f_0}. \quad (\text{B.1})$$

At critical coupling $Q = Q_L = 36$, yielding $\tau_{\text{ring}} = 4$ ns.

2. Electric Field Simulation

Ideally, the electric fields of the TE_{01} cavity mode are completely confined within the LGR capacitive gaps, ensuring that f_0 remains constant when differently-sized diamonds are placed within the central loop. In practice, fringing electric fields from the capacitive gaps extend partially into the LGR's central loop as shown in

Fig. B.1. However, at distances > 1 mm from the capacitive gaps, the electric field magnitude E is decreased by $> 10\times$ from the peak field inside the capacitive gap. Consequently, insertion of a diamond (with $\epsilon_r \approx 5.7$ at 3 GHz⁸⁶) beyond this region has little if any effect on the LGR resonant frequency f_0 .

3. Axial Field Uniformity

Figure B.2 plots the simulated magnitude of B_1 along the LGR's symmetry axis, illustrating the improved axial field uniformity possible with three-dimensional cavity resonators^{50,52,53}, compared to that of planar-only geometries. The presence of the split ring resonator at $z = 4.024$ mm perturbs B_1 inside the LGR, shifting the point of maximal B_1 down by 0.4 mm, away from the split ring resonator. Within a cylindrical volume of 3.14 mm^3 (1 mm radius and 1 mm thickness), centered around the point of maximal B_1 , the simulation predicts $\sigma_{\text{rms}} = 0.78\%$ and $\sigma_{\text{pp}} = 3.7\%$. For a larger cylindrical volume of 12.6 mm^3 (2 mm radius and 1 mm thickness), the simulation predicts $\sigma_{\text{rms}} = 2\%$ and $\sigma_{\text{pp}} = 8\%$. These dimensions are comparable to those of commercially available single-crystal diamonds.

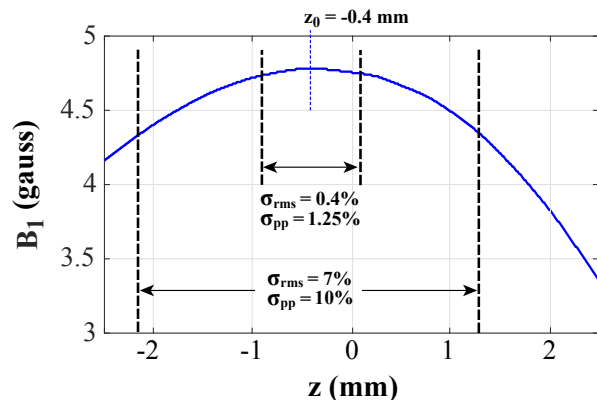


FIG. B.2. (Color online) **Simulated B_1 field along LGR symmetry axis.** The symmetry plane of the LGR is located at $z = 0$ mm. The edges of the LGR are at $z = \pm 2.5$ mm, and the split-ring resonator is located at position $z = 4.0$ mm. The presence of the split-ring resonator shifts the point of maximal B_1 off center to $z_0 = -0.4$ mm.

4. Smaller Cavity Measurement

To achieve stronger MW driving, we also designed and fabricated smaller LGR with central loop radius $r_c = 2.5$ mm and $n = 4$ outer loops of radius $r_0 = 2.45$ mm, as shown in Fig. B.3(a). The naked air-gapped LGR cavity exhibits $f_0 = 4.5$ GHz, similar to the larger LGR design described in the main text. Employing the same exciter antenna from Section III, we measure $B_1 = 5.8$ G at the center of the smaller LGR device. Figure B.3(b) depicts S_{11} for the composite device; the measured 3dB bandwidth $\Delta_{3\text{dB}} = 113$ MHz corresponds to a loaded quality factor $Q_L = 25$, and an associated ring-down time of 2.8 ns.

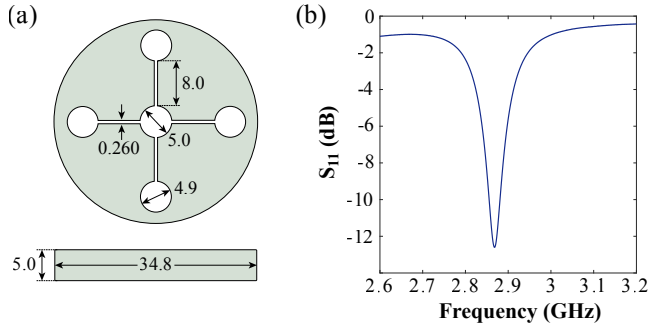


FIG. B.3. (Color online) **Smaller LGR design.** (a) Line drawing of smaller LGR with central loop radius $r_c = 2.5$ mm as described in Section B 4. Units are in mm. (b) Measured S_{11} for composite device tuned to $f_0 \approx 2.87$ GHz.

- ¹T. Gaebel, M. Domhan, I. Popa, C. Wittmann, P. Neumann, F. Jelezko, J. R. Rabeau, N. Stavrias, A. D. Greentree, S. Praver, J. Meijer, J. Twamley, P. R. Hemmer, and J. Wrachtrup, *Nature Physics* **2**, 408 (2006), [quant-ph/0605038](#).
- ²M. V. G. Dutt, L. Childress, L. Jiang, E. Togan, J. Maze, F. Jelezko, A. S. Zibrov, P. R. Hemmer, and M. D. Lukin, *Science* **316** (2007), [10.1126/science.1139831](#).
- ³G. Waldherr, P. Neumann, S. F. Huelga, F. Jelezko, and J. Wrachtrup, *Physical Review Letters* **107**, 090401 (2011).
- ⁴B. Hensen, N. Kalb, M. S. Blok, A. E. Dréau, A. Reiserer, R. F. L. Vermeulen, R. N. Schouten, M. Markham, D. J. Twitchen, K. Goodenough, D. Elkouss, S. Wehner, T. H. Taminiau, and R. Hanson, *Scientific Reports* **6**, 30289 (2016), [arXiv:1603.05705 \[quant-ph\]](#).
- ⁵J. M. Taylor, P. Cappellaro, L. Childress, L. Jiang, D. Budker, P. R. Hemmer, A. Yacoby, R. Walsworth, and M. D. Lukin, *Nature Physics* **4**, 810 (2008), [arXiv:0805.1367 \[cond-mat.mes-hall\]](#).
- ⁶F. Dolde, H. Fedder, M. W. Doherty, T. Nöbauer, F. Rempp, G. Balasubramanian, T. Wolf, F. Reinhard, L. C. L. Hollenberg, F. Jelezko, and J. Wrachtrup, *Nature Physics* **7**, 459 (2011), [arXiv:1103.3432 \[quant-ph\]](#).
- ⁷E. H. Chen, H. A. Clevenson, K. A. Johnson, L. M. Pham, D. R. Englund, P. R. Hemmer, and D. A. Braje, *Phys. Rev. A* **95**, 053417 (2017).
- ⁸S. J. Devience, L. M. Pham, I. Lovchinsky, A. O. Sushkov, N. Bar-Gill, C. Belthangady, F. Casola, M. Corbett, H. Zhang, M. Lukin, H. Park, A. Yacoby, and R. L. Walsworth, *Nature Nanotechnology* **10**, 129 (2015), [arXiv:1406.3365 \[quant-ph\]](#).
- ⁹P. Kehayias, A. Jarmola, N. Mosavian, I. Fescenko, F. M. Benito, A. Laraoui, J. Smits, L. Bougas, D. Budker, A. Neumann, S. R. J. Brueck, and V. M. Acosta, *Nature Communications* **8**, 188 (2017), [arXiv:1701.01401 \[cond-mat.mes-hall\]](#).
- ¹⁰D. B. Bucher, D. R. Glenn, J. Lee, M. D. Lukin, H. Park, and R. L. Walsworth, ArXiv e-prints (2017), [arXiv:1705.08887 \[quant-ph\]](#).
- ¹¹A. O. Sushkov, I. Lovchinsky, N. Chisholm, R. L. Walsworth, H. Park, and M. D. Lukin, *Physical Review Letters* **113**, 197601 (2014), [arXiv:1410.1355 \[quant-ph\]](#).
- ¹²I. Lovchinsky, A. O. Sushkov, E. Urbach, N. P. de Leon, S. Choi, K. De Greve, R. Evans, R. Gertner, E. Bersin, C. Müller, L. McGuinness, F. Jelezko, R. L. Walsworth, H. Park, and M. D. Lukin, *Science* **351**, 836 (2016).
- ¹³P. Neumann, I. Jakobi, F. Dolde, C. Burk, R. Reuter, G. Waldherr, J. Honert, T. Wolf, A. Brunner, J. H. Shim, D. Suter, H. Sumiya, J. Isoya, and J. Wrachtrup, *Nano Letters* **13**, 2738 (2013), [arXiv:1304.0688 \[quant-ph\]](#).
- ¹⁴G. Kucsko, P. C. Maurer, N. Y. Yao, M. Kubo, H. J. Noh, P. K. Lo, H. Park, and M. D. Lukin, *Nature Physics* **500**, 54 (2013), [arXiv:1304.1068 \[quant-ph\]](#).
- ¹⁵J. S. Hodges, N. Y. Yao, D. Maclaurin, C. Rastogi, M. D. Lukin, and D. Englund, *Physical Review A* **87**, 032118 (2013).
- ¹⁶J. F. Barry, M. J. Turner, J. M. Schloss, D. R. Glenn, Y. Song, M. D. Lukin, H. Park, and R. L. Walsworth, *Proceedings of the National Academy of Science* **113**, 14133 (2016), [arXiv:1602.01056 \[quant-ph\]](#).
- ¹⁷A. Laraoui, H. Aycock-Rizzo, Y. Gao, X. Lu, E. Riedo, and C. A. Meriles, *Nature Communications* **6**, 8954 (2015), [arXiv:1511.06916 \[cond-mat.mes-hall\]](#).
- ¹⁸J.-P. Tetienne, N. Dontschuk, D. A. Broadway, A. Stacey, D. A. Simpson, and L. C. L. Hollenberg, *Science Advances* **3**, e1602429 (2017), [arXiv:1609.09208 \[cond-mat.mes-hall\]](#).
- ¹⁹E. van Oort, N. B. Manson, and M. Glasbeek, *Journal of Physics C Solid State Physics* **21**, 4385 (1988).
- ²⁰A. P. Nizovtsev, S. Y. Kilin, F. Jelezko, I. Popa, A. Gruber, and J. Wrachtrup, *Physica B Condensed Matter* **340**, 106 (2003).
- ²¹G. Balasubramanian, I. Chan, R. Kolesov, M. Al-Hmoud, J. Tisler, C. Shin, C. Kim, A. Wojcik, P. R. Hemmer, A. Krueger, *et al.*, *Nature* **455**, 648 (2008).
- ²²N. Bar-Gill, L. M. Pham, A. Jarmola, D. Budker, and R. L. Walsworth, *Nature Communications* **4**, 1743 (2013), [arXiv:1211.7094 \[quant-ph\]](#).
- ²³B. A. Myers, A. Ariyaratne, and A. C. B. Jayich, *Physical Review Letters* **118**, 197201 (2017), [arXiv:1607.02553 \[cond-mat.mes-hall\]](#).
- ²⁴E. Bauch, C. A. Hart, J. M. Schloss, M. J. Turner, J. F. Barry, P. Kehayias, S. Singh, and R. L. Walsworth, ArXiv e-prints (2018), [arXiv:1801.03793 \[quant-ph\]](#).
- ²⁵C. L. Degen, *Applied Physics Letters* **92**, 243111 (2008), [arXiv:0805.1215](#).
- ²⁶P. Maletinsky, S. Hong, M. S. Grinolds, B. Hausmann, M. D. Lukin, R. L. Walsworth, M. Loncar, and A. Yacoby, *Nature Nanotechnology* **7**, 320 (2012), [arXiv:1108.4437 \[cond-mat.mes-hall\]](#).
- ²⁷B. J. Maertz, A. P. Wijnheijmer, G. D. Fuchs, M. E. Nowakowski, and D. D. Awschalom, *Applied Physics Letters* **96**, 092504 (2010), [arXiv:0912.1355 \[cond-mat.mes-hall\]](#).
- ²⁸H. Clevenson, L. M. Pham, C. Teale, K. Johnson, D. Englund, and D. Braje, ArXiv e-prints (2018), [arXiv:1802.09713 \[quant-ph\]](#).
- ²⁹J. M. Schloss, J. F. Barry, M. J. Turner, and R. L. Walsworth, ArXiv e-prints (2018), [arXiv:1803.03718 \[quant-ph\]](#).
- ³⁰A. Wickenbrock, H. Zheng, L. Bougas, N. Leefer, S. Afach, A. Jarmola, V. M. Acosta, and D. Budker, *Applied Physics Letters* **109**, 053505 (2016), [arXiv:1606.03070 \[cond-mat.mes-hall\]](#).
- ³¹R. Akhmedzhanov, L. Gushchin, N. Nizov, V. Nizov, D. Sobgayda, I. Zelensky, and P. Hemmer, *Physical Review A* **96**, 013806 (2017).
- ³²D. Le Sage, K. Arai, D. Glenn, S. DeVience, L. Pham, L. Rahn-Lee, M. Lukin, A. Yacoby, A. Komeili, and R. Walsworth, *Nature* **496**, 486 (2013).
- ³³D. R. Glenn, R. R. Fu, P. Kehayias, D. Le Sage, E. A. Lima, B. P. Weiss, and R. L. Walsworth, *Geochemistry, Geophysics, Geosystems* (2017).
- ³⁴R. R. Fu, B. P. Weiss, E. A. Lima, R. J. Harrison, X.-N. Bai, S. J. Desch, D. S. Ebel, C. Suavet, H. Wang, D. Glenn, D. Le Sage, T. Kasama, R. L. Walsworth, and A. T. Kuan, *Science* **346**, 1089 (2014), [http://www.sciencemag.org/content/346/6213/1089.full.pdf](#).
- ³⁵T. Wolf, P. Neumann, K. Nakamura, H. Sumiya, T. Ohshima, J. Isoya, and J. Wrachtrup, *Physical Review X* **5**, 041001 (2015), [arXiv:1411.6553 \[quant-ph\]](#).
- ³⁶H. Clevenson, M. E. Trusheim, C. Teale, T. Schröder, D. Braje, and D. Englund, *Nature Physics* **11**, 393 (2015), [arXiv:1406.5235 \[quant-ph\]](#).
- ³⁷M. Chipaux, A. Tallaire, J. Achard, S. Pezzagna, J. Meijer, V. Jacques, J.-F. Roch, and T. Debuisschert, *European Physical Journal D* **69**, 166 (2015), [arXiv:1410.0178 \[cond-mat.mes-hall\]](#).
- ³⁸P. Andrich, F. Charles, X. Liu, H. L. Bretscher, J. R. Berman, F. J. Heremans, P. F. Nealey, and D. D. Awschalom, *npj Quantum Information* **3**, 28 (2017).
- ³⁹N. Zhang, C. Zhang, L. Xu, M. Ding, W. Quan, Z. Tang, and H. Yuan, *Applied Magnetic Resonance* **47**, 589 (2016).
- ⁴⁰C. Zhang, H. Yuan, N. Zhang, L. Xu, J. Zhang, B. Li, and J. Fang, *Journal of Physics D: Applied Physics* **51**, 155102 (2018).
- ⁴¹M. Mrózek, J. Mlynarczyk, D. S. Rudnicki, and W. Gawlik, *Applied Physics Letters* **107**, 013505 (2015), [arXiv:1503.04612 \[physics.atom-ph\]](#).

- ⁴²K. Bayat, J. Choy, M. Farrokh Baroughi, S. Meesala, and M. Loncar, *Nano Letters* **14**, 1208 (2014).
- ⁴³K. Sasaki, Y. Monnai, S. Saijo, R. Fujita, H. Watanabe, J. Ishi-Hayase, K. M. Itoh, and E. Abe, *Review of Scientific Instruments* **87**, 053904 (2016).
- ⁴⁴Y. Twig, E. Suhovoy, and A. Blank, *Review of Scientific Instruments* **81**, 104703-104703-11 (2010).
- ⁴⁵V. R. Horowitz, B. J. Alemán, D. J. Christle, A. N. Cleland, and D. D. Awschalom, *Proceedings of the National Academy of Science* **109**, 13493 (2012), arXiv:1206.1573 [cond-mat.mtrl-sci].
- ⁴⁶A. Horsley, P. Appel, J. Wolters, J. Achard, A. Tallaire, P. Maletinsky, and P. Treutlein, ArXiv e-prints (2018), arXiv:1802.07402 [quant-ph].
- ⁴⁷D. A. Simpson, R. G. Ryan, L. T. Hall, E. Panchenko, S. C. Drew, S. Petrou, P. S. Donnelly, P. Mulvaney, and L. C. L. Hollenberg, *Nature Communications* **8**, 458 (2017).
- ⁴⁸B. C. Rose, A. M. Tyryshkin, H. Riemann, N. V. Abrosimov, P. Becker, H.-J. Pohl, M. L. W. Thewalt, K. M. Itoh, and S. A. Lyon, *Physical Review X* **7**, 031002 (2017), arXiv:1702.00504 [quant-ph].
- ⁴⁹J. D. Breeze, J. Sathian, E. Salvadori, N. McN. Alford, and C. W. M. Kay, ArXiv e-prints (2017), arXiv:1710.07726.
- ⁵⁰J.-M. Le Floch, N. Delhote, M. Aubourg, V. Madrangeas, D. Cros, S. Castelletto, and M. E. Tobar, *Journal of Applied Physics* **119**, 153901 (2016), arXiv:1604.01516 [quant-ph].
- ⁵¹D. L. Creedon, J.-M. Le Floch, M. Goryachev, W. G. Farr, S. Castelletto, and M. E. Tobar, *Physical Review B* **91**, 140408 (2015), arXiv:1412.4331 [cond-mat.mes-hall].
- ⁵²P. Kapitanova, V. Soshenko, V. Vorobyov, D. Dobrykh, S. Bolshedvorskiih, V. Sorokin, and A. Akimov, in *American Institute of Physics Conference Series*, American Institute of Physics Conference Series, Vol. 1874 (2017) p. 030017.
- ⁵³A. Angerer, T. Astner, D. Wirtitsch, H. Sumiya, S. Onoda, J. Isoya, S. Putz, and J. Majer, *Applied Physics Letters* **109**, 033508 (2016), arXiv:1605.05554 [quant-ph].
- ⁵⁴M. W. Doherty, N. B. Manson, P. Delaney, F. Jelezko, J. Wrachtrup, and L. C. L. Hollenberg, *Physics Reports* **528**, 1 (2013), arXiv:1302.3288 [cond-mat.mtrl-sci].
- ⁵⁵R. Schirhagl, K. Chang, M. Loretz, and C. L. Degen, *Annual Review of Physical Chemistry* **65**, 83 (2014).
- ⁵⁶H. C. Davis, P. Ramesh, A. Bhatnagar, A. Lee-Gosselin, J. F. Barry, D. R. Glenn, R. L. Walsworth, and M. G. Shapiro, *Nature Communications* **9**, 131 (2018).
- ⁵⁷D. R. Glenn, K. Lee, H. Park, R. Weissleder, A. Yacoby, M. D. Lukin, H. Lee, R. L. Walsworth, and C. B. Connolly, *Nature methods* **12**, 736 (2015).
- ⁵⁸D. A. Simpson, J.-P. Tetienne, J. M. McCoe, K. Ganesan, L. T. Hall, S. Petrou, R. E. Scholten, and L. C. L. Hollenberg, *Scientific Reports* **6**, 22797 (2016), arXiv:1508.02135 [cond-mat.mes-hall].
- ⁵⁹V. M. Acosta, E. Bauch, M. P. Ledbetter, C. Santori, K.-M. C. Fu, P. E. Barclay, R. G. Beausoleil, H. Linget, J. F. Roch, F. Treussart, S. Chemerisov, W. Gawlik, and D. Budker, *Physical Review B* **80**, 115202 (2009), arXiv:0903.3277 [cond-mat.mtrl-sci].
- ⁶⁰G. Chatzidrosos, A. Wickenbrock, L. Bougas, N. Leefer, T. Wu, K. Jensen, Y. Dumeige, and D. Budker, *Phys. Rev. Applied* **8**, 044019 (2017).
- ⁶¹R. L. Wood, W. Froncisz, and J. S. Hyde, *Journal of Magnetic Resonance* **58**, 243 (1984).
- ⁶²W. Froncisz and J. S. Hyde, *Journal of Magnetic Resonance* **47**, 515 (1982).
- ⁶³W. Froncisz, T. Oles, and J. S. Hyde, *Review of Scientific Instruments* **57**, 1095 (1986).
- ⁶⁴W. Piasecki and W. Froncisz, *Measurement Science and Technology* **4**, 1363 (1993).
- ⁶⁵A. S. W. B. Westphal, *Dielectric Constant and Loss Data* (Air Force Materials Laboratory, Air Force Systems Command, 1972).
- ⁶⁶J. G. Hartnett, M. E. Tobar, E. N. Ivanov, and J. Krupka, *IEEE Transactions on Ultrasonics, Ferroelectrics, and Frequency Control* **53**, 34 (2006).
- ⁶⁷M. F. Koskinen and K. R. Metz, *Journal of Magnetic Resonance* **98**, 576 (1992).
- ⁶⁸L. M. Pham, *Magnetic field sensing with nitrogen-vacancy color centers in diamond*, Ph.D. thesis, Harvard University (2013).
- ⁶⁹L. I. Childress, *Coherent manipulation of single quantum systems in the solid state*, Ph.D. thesis, Harvard University (March 2007).
- ⁷⁰J. Maze Rios, *Quantum manipulation of nitrogen-vacancy centers in diamond: From basic properties to applications*, Ph.D. thesis, Harvard University (2010).
- ⁷¹Y. Tabuchi, M. Negoro, K. Takeda, and M. Kitagawa, *Journal of Magnetic Resonance* **204**, 327 (2010).
- ⁷²T. W. Borneman and D. G. Cory, *Journal of Magnetic Resonance* **225**, 120 (2012), arXiv:1207.1139 [quant-ph].
- ⁷³A. S. Peshkovsky, J. Forgue, L. Cerioni, and D. J. Pusiol, *Journal of Magnetic Resonance* **177**, 67 (2005).
- ⁷⁴S. Pfenninger, W. Froncisz, J. Forrer, J. Luglio, and J. S. Hyde, *Review of Scientific Instruments* **66**, 4857 (1995).
- ⁷⁵G. A. Rinard and G. R. Eaton, *Biomedical EPR, Part B: Methodology, Instrumentation, and Dynamics* (Kluwer Academic/Plenum Publishers, 2005) pp. 19–52.
- ⁷⁶B. Smeltzer, J. McIntyre, and L. Childress, *Physical Review A* **80**, 050302 (2009), arXiv:0909.3896 [quant-ph].
- ⁷⁷F. Jelezko, T. Gaebel, I. Popa, A. Gruber, and J. Wrachtrup, *Physical Review Letters* **92**, 076401 (2004).
- ⁷⁸Y. Twig, E. Dikarov, and A. Blank, *Molecular Physics* **111**, 2674 (2013).
- ⁷⁹N. Haider Protik, A. Katre, L. Lindsay, J. Carrete, N. Mingo, and D. Broido, ArXiv e-prints (2017), arXiv:1705.02634 [cond-mat.mtrl-sci].
- ⁸⁰X. Qian, P. Jiang, and R. Yang, ArXiv e-prints (2017), arXiv:1712.00830 [cond-mat.mtrl-sci].
- ⁸¹S. Karaveli, O. Gaathon, A. Wolcott, R. Sakakibara, O. A. Shemesh, D. S. Peterka, E. S. Boyden, J. S. Owen, R. Yuste, and D. Englund, *Proceedings of the National Academy of Science* **113**, 3938 (2016).
- ⁸²Y. Wu, F. Jelezko, M. B. Plenio, and T. Weil, *Angewandte Chemie International Edition* **55**, 6586 (2016).
- ⁸³J. R. Maze, A. Gali, E. Togan, Y. Chu, A. Trifonov, E. Kaxiras, and M. D. Lukin, *New Journal of Physics* **13**, 025025 (2011), arXiv:1010.1338 [quant-ph].
- ⁸⁴K. Jensen, P. Kehayias, and D. Budker, in *High Sensitivity Magnetometers* (Springer, 2017) pp. 553–576.
- ⁸⁵L. Rondin, J.-P. Tetienne, T. Hingant, J.-F. Roch, P. Maletinsky, and V. Jacques, *Reports on Progress in Physics* **77**, 056503 (2014), arXiv:1311.5214 [cond-mat.mes-hall].
- ⁸⁶A. Ibarra, M. González, R. Vila, and J. Mollá, *Diamond and Related Materials* **6**, 856 (1997).